ARTICLE

New Insights into Controlling the Functional Properties of Tin Oxide-Based Materials

Alexandra Kuriganova*, Nina Smirnova

Platov South Russian State Polytechnic University (NPI), Novocherkassk 346428, Russia

Abstract

Development of methodologies for fabrications of nanostructured materials that provide control over their microstructural features and compositions represents a fundamental step in the advancement of technologies for productions of materials with well-defined functional properties. Pulse electrolysis, a top-down electrochemical approach, has been demonstrated to be a viable method for producing nanostructured materials with a particular efficacy in the synthesis of tin oxides. This method allows for significant control over the composition and shape of the resulting tin oxides particles by modifying the anionic composition of the aqueous electrolyte, obviating the need for additional capping agents in the synthesis process and eliminating the requirement for high-temperature post-treatments. The composition and microstructural characteristics of these oxides are found to be contingent upon the differing stabilities of tin fluoride and chloride complexes, as well as the distinct mechanisms of interaction between chloride and fluoride anions with an oxidized tin surface, which is influenced by the varying kosmotropic/chaotropic nature of these anions. The composition and microstructural characteristics of the obtained dispersed tin oxides would thus determine their potential applications as an anode material for lithium-ion batteries, as a photocatalyst, or as an oxyphilic component of a hybrid support for a platinum-containing electrocatalyst.

Keywords: Tin oxide; Pulse electrolysis; Lithium-ion battery; Photocatalysis; Fuel cell

1. Introduction

The science of semiconductor materials has undergone a profound evolution in recent decades, driven by the distinctive physical and chemical properties of these materials [1–4]. Among them, metal oxides and, in particular, tin oxide-based nanostructures, have attracted much attention due to their potential applications in environmental catalysis technologies, and energy storage and conversion devices [5–8]. The wide band gap (3.6–3.8 eV) and high transparency in the visible region of the spectrum render tin oxides effective materials for advanced oxidation processes – photoelectrocatalysis, photodegradation of organic pollutants [9, 10]. High theoretical capacity with faster lithiation/delithiation kinetics of tin oxide (SnO_x) allows for the consideration of this material as a promising anode for lithium-ion batteries (LIBs) [6]. The ability to provide a more efficient supply of oxygen-containing particles for the adsorption of ethanol via dehydrogenative processes renders SnO_x a valuable component in platinum (Pt)-containing catalysts employed in direct ethanol oxidation fuel cells (DEFCs) technology [8, 11].

The efficacy of SnO_x materials in the aforementioned application is contingent upon their morphological characteristics [12, 13]. For instance, it has been demonstrated that varying the size of tin dioxide (SnO_2) nanoparticles by changing the composition of the initial components during the hydrothermal synthesis resulted in a concomitant reduction in both the band gap and surface energy states, thereby limiting the photocatalytic activity of the material [13]. The synthesis of SnO_2 nanoparticles via the co-precipitation technique [14] allows for the production of nanoparticles with adjustable crystallite size and band gap. These properties will undoubtedly affect the functional properties of the resulting materials. The sol-gel method, utilising a biological egg membrane as a template, has led to a notable enhancement in the electrochemical performance of

Received 26 August 2024; Received in revised form 14 October 2024; Accepted 12 November 2024
Available online 14 November 2024

*Corresponding Author, E-mail: kuriganova_@mail.ru

https://doi.org/10.61558/2993-074X.3509

SnO_2-based materials [15]. This is attributed to the restriction of active particle mobility during repeated cycling, the provision of sufficient space for volume change during the lithiation/delithiation process, the reduction in the solid-state diffusion length for Li^+ insertion, and the facilitation of liquid electrolyte diffusion into the electrode's bulk. These factors collectively result in an improvement in the electrode's kinetics. The controlling mesopore sizes in the range of 4–11 nm of the mesoporous antimony (Sb)-doped tin oxides supports in the composition of the Pt-containing catalyst as the cathodes of polymer electrolyte fuel cells allow the establishment that the higher fuel cell performance was observed at a pore size of 7.3 nm [11].

In the case of any nanostructured material, the research focusing on tin oxides is the development of methods for tailoring the material for specific applications. This can be achieved through the control of its composition, microstructural characteristics and crystallographic properties. The synthesis of tin oxide-based nanostructures can be achieved through a variety of traditional methods, including physical methods such as thermal deposition and chemical vapor deposition, as well as chemical methods such as sol-gel, hydrothermal, solvothermal, and template-based precipitation. The technological bases, advantages, and disadvantages of these methods have been discussed in detail in the published review [3].

Despite the potential for the synthesis of nanostructures with different dimensions based on tin oxides [16], it is challenging to achieve the SnO_x structures formed with distinct morphologies or compositions through a single approach to material synthesis. In the present study, we have investigated the potential of an electrochemical top-down synthesis approach to variate the composition and morphology of SnO_x structures. This electrochemical top-down approach is based on the oxidation/destruction of metal electrodes in aqueous electrolytes under the action of pulse alternating current which has been successfully applied for many times on the synthesis of nanomaterials with a wide range of d-metals [17–31], p-metals (including Sn) [32–35] and carbon materials [36, 37] for a wide range of applications. This methodology enables the production of crystal metal oxides, including those in a crystalline form and a single stage, circumventing the necessity for thermal post-treatment of the material. Furthermore, the synthesis parameters, including the electrolyte composition and electric current, can be varied in certain instances to modify the size, morphology, and composition of nanostructured materials obtained under conditions of pulse electrolysis.

Previously, we have demonstrated the potential of pulsed electrolysis to produce SnO_x-based materials [32, 33, 38–40]. The objective of the present study was to establish the fundamental principles of controlling the functionality of tin oxide-based materials by varying their composition and microstructure under conditions of electrochemical top-down synthesis.

2. Experimental Section

2.1. Synthesis of tin oxide-based materials through an electrochemical top-down approach

The synthesis of SnO_x powders was conducted in accordance with the following procedure: two tin-plate electrodes with a geometric surface area of 6 cm^2 each were placed in an aqueous electrolyte solution (1 $mol \cdot L^{-1}$ NaCl or 1 $mol \cdot L^{-1}$ NaF). An alternating pulsed current with a frequency of 50 Hz and an average current density of 1.0 $A \cdot cm^{-2}$ was applied to the tin electrodes. The alternating pulse current induced the dissolution/destruction of the tin electrodes, accompanied by the formation of dispersed SnO_x particles within the electrolyte volume. The synthesis was conducted in a jacketed cell and under constant stirring with a magnetic stirrer. Once the synthesis process was complete, the SnO_x suspension was filtered and the SnO_x powder was repeatedly washed with double distilled water. The resulting powder was then air-dried at 80 °C until it reached a constant mass (Fig. 1a). Hereinafter, the SnO_x obtained in 1 $mol \cdot L^{-1}$

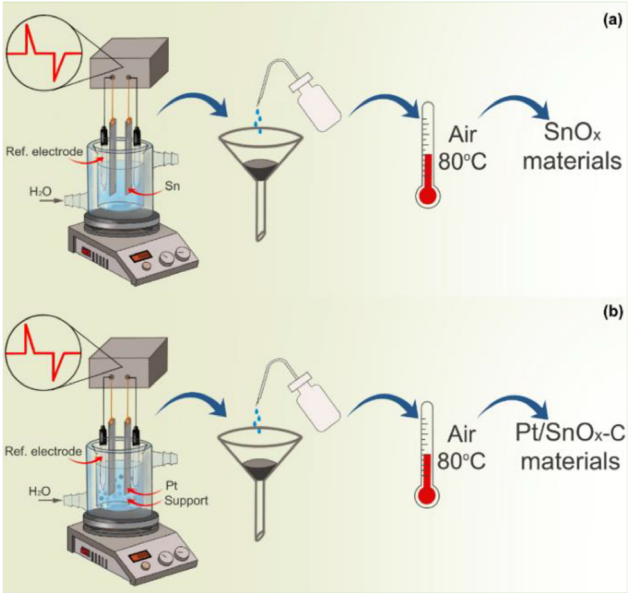

Fig. 1. Schematic illustrations for the synthesis of SnO_x-based materials (a) and SnO_x-carbon supported platinum materials (b) under pulse electrolysis conditions.

NaCl electrolyte will be referred to as $SnO_{x(Cl)}$, and in 1 mol·L^{-1} NaF electrolyte as $SnO_{x(F)}$.

The synthesis of Pt/SnO_x-C materials was carried out in accordance with the methodology described in [38]. Two Pt electrodes were placed in a suspension of $SnO_{x(Cl)}$ or $SnO_{x(F)}$ material and Vulcan XC-72 carbon black in an aqueous solution of 1 mol·L^{-1} NaOH. An alternating pulsed current with a frequency of 50 Hz and an average current density of 1.0 A·cm^{-2} was applied to the Pt electrodes. The Pt electrodes were destructed under the action of alternating pulsed current, forming the Pt nanoparticles, which were immediately deposited on the surface of the SnO_x-C hybrid support. In a manner analogous to the synthesis of SnO_x, the process was conducted with a constant stirring and cooling of the electrolyte. Following synthesis, the suspension of Pt/SnO_x-C materials was filtered, and the resulting catalyst was washed repeatedly with double distilled water and air-dried at 80 °C until a constant mass was achieved (Fig. 1b). Hereinafter, the Pt/SnO_x-C materials obtained using $SnO_{x(Cl)}$ and $SnO_{x(F)}$ will be referred to as Pt/$SnO_{x(Cl)}$-C and Pt/$SnO_{x(F)}$-C, respectively.

2.2. Physico-chemical characterizations

X-ray diffraction (XRD) analysis was performed on the Swiss-Norwegian Beamlines (SNBL) of the ESRF (Grénoble, France) in the Debye-Scherrer geometry at a radiation wavelength λ of 0.7121 Å using a 2-D Pilatus2M (Dectris) detector. The study of the chemical composition of the samples surface was carried out on a photoelectron spectrometer of SPECS Surface Nano Analysis GmbH (Germany), equipped with a hemispherical analyser PHOIBOS-150-MCD-9 and a source of X-ray characteristic radiation XR-50 with a double Al/Mg anode. Non-monochromatised radiation from Al K_α (h^* = 1486.6 eV) was used to record the spectra. Thermogravimetric analysis (TGA) and differential scanning calorimetric (DSC) analyses were carried out using Mettler Toledo TGA/DSC 1 in the range of 25–1000 °C at a heating rate of 10 °C·min^{-1} under an air atmosphere. The low-temperature N_2 adsorption and desorption measurements were made on a QUADRASORB SI unit at 77 K. All the investigated samples were degassed at 573 K for 2 h in a vacuum prior to the adsorption experiment. The specific surface area based on Brunauer-Emmett-Teller (S_{BET}) was determined at the relative pressure (P/P_0) values of $P/P_0 \leq 0.3$. The total pore volume was calculated from the N_2 adsorption isotherm at $P/P_0 \rightarrow 1$. The pore size distribution was analyzed in the context of the Barrett-Joyner-Halenda (BJH) method. The morphology of samples was inspected in a Hitachi HT7700 transmission electron microscope. The images were acquired in the bright-field transmission electron microscope (TEM) mode at a 100 kV accelerating voltage. Scanning electron microscopy (SEM) was employed to study surface morphology of samples by using a Hitachi S-3400N electron microscope.

2.3. LIBs performance tests

Electrochemical characterization of the anode SnO_x material was carried out by galvanostatic cycling using a P45X potentiostat/galvanostat (Electrochemical instruments, Russia). The galvanostatic measurements were made using coin-type cells, closed by a hydraulic crimping machine (MSK 110 from MTI Corporation). The cell assembly, coin cells crimping, was performed at room temperature in a glove-box with H_2O and O_2 levels below 0.1 ppm. All the measurements were performed using a standard electrolyte solution 1 mol·L^{-1} $LiPF_6$ in EC:DMC (1:1).

2.4. Photocatalysis measurements

The photocatalysis experiments were performed with methylene blue (MB) solution (10 ppm, 50 mL) containing the catalyst (50 mg). A Hamamatsu LC8 Mercury-Xenon UV-VIS combined lamp (Hamamatsu Photonics, Shizuoka) with the main irradiation wavelength of 365 nm was used as the light source. Prior to UV irradiation, the solution was ultrasonically treated and then stirred for 30 min under darkness to reach the adsorption-desorption equilibrium of the dye on the photocatalyst surface. The dye solution was exposed to UV irradiation under constant stirring. The aliquots (2 mL) were sampled after time intervals of 10 min and analyzed for variations in the absorbance at 664 nm of MB dye using a Shimadzu UV-1800 UV-VIS spectrophotometer.

2.5. Lectrocatalysis measurements

The "catalytic ink" contained the synthesized Pt/SnO_x-C electrocatalysts, 10% Nafion® DE-1020 solution and isopropanol. All the electrochemical measurements were carried out in a standard three-electrode cell. The preparation of the working electrode included dropping the catalytic ink onto a glassy carbon plate and drying the electrode in an air. A platinum wire was used as the counter electrode. Ag/AgCl electrode was used as the reference electrode. All potentials were then recalculated on the scale of a reversible hydrogen electrode (RHE). Before starting all electrochemical measurements, the working electrode was cycled for 30 times in 0.5 mol·L^{-1} H_2SO_4 over a potential range of 0.05–1.5 V with a scan rate 0.02 V·s^{-1}.

Electrochemical cycling performance tests were implemented in a three-electrode cell in 0.5 mol·L^{-1} H_2SO_4 containing 0.5 mol·L^{-1} C_2H_5OH deaerated with N_2 over a potential range of 0.05–1.5 V. Comparison of CVs was carried out after preliminary cycling of the working electrode for 20 cycles. The electrochemically active surface area (ECSA) of the electrocatalysts was determined by CO-stripping. CO was preliminarily adsorbed on the working electrode at a potential of 0.3 V vs. RHE in dearated 0.5 mol·L^{-1} H_2SO_4 electrolyte. Then, CO was removed from the electrolyte by purging the electrolyte with N_2, and the CV curve of the electrode was measured from 0.3 V. A CO desorption peak was observed in the first cycle. Based on the charge used for CO desorption, the ECSA of Pt-containing particles is calculated according to the following equation.

$$\mathrm{ECSA} = \frac{Q_{\mathrm{CO}}}{Q_m \times g_{Pt}} \quad (1)$$

where Q_{CO} is the charge passed during the CO oxidation, g_{Pt} is the mass of Pt-containing phase on the working electrode and Q_m (= 420 μC·cm^{-2}) [41] is the charge required for the desorption of a CO_{ads} monolayer.

3. Results and Discussion

3.1. Synthesis and physico-chemical characterizations of SnO_x-based materials

It is well established that under anodic polarization conditions, tin is readily oxidized to form various dispersed oxide forms of tin [42]. The application of an alternating pulse current at a frequency of 50 Hz to tin electrodes in an alkaline electrolyte did not result in the formation of dispersed products (Table 1). This may be attributed to the passivation of the tin electrode surface, which is thought to the result from the formation of a tin oxide (IV) film. This film is known to possess n-type semiconductor properties [43]. In contrast, the formation of dispersed products was observed to be more intense in electrolytes containing halogen ions when an alternating pulse current was applied. The rate of this process was found to depend on the type of electrolyte anion and the average current density (j_{av}) (Table 1).

The highest formation rate of tin electrode dispersion products (180.3 ± 6.3 mg (cm^{-2}·h^{-1})) under pulse electrolysis conditions was observed at a current density of 1.0 A·cm^{-2} when using an electrolyte that contains $C1^-$ anions. In contrast, the lowest rate of formation (56.5 ± 3.0 mg (cm^{-2}·h^{-1})) was observed when using an electrolyte that contains F^- anions.

Previously [35, 44], we have demonstrated that the SnO_x materials prepared in both NaF and NaCl solutions contained the peaks corresponding to the tetragonal SnO phase with a space group P4/nmm and those of SnO_2 with a space group P42/mnm. In addition to these phases, the XRD pattern of $SnO_{x(F)}$ sample synthesized in a NaF solution exhibited the low-intensity peaks assigned to tetragonal phases P-421c of tin(II) oxyhydroxide $Sn_6O_4(OH)_4$ (~1%) [45] and *β*-Sn with a space group I4/mmm. The $SnO_{x(Cl)}$ sample was almost entirely composed of SnO_2 nanoparticles whose average size was 7.6 nm (~96% of SnO_2 phase and >3% of SnO phase). In turn, the $SnO_{x(F)}$ sample possessed the predominance of SnO (~12% of SnO_2 phase and ~85% of SnO phase, ~2% of *β*-Sn and ~1% of $Sn_6O_4(OH)_4$ phase) (Figure S1, Table 1). It is also important to consider the potential doping of SnO_x with chlorine and fluorine during the pulse electrolysis, a hypothesis that has been previously confirmed through the Raman spectroscopy [35].

The TGA results (Fig. 2a) indicate that the material obtained in a NaF electrolyte ($SnO_{x(F)}$) is characterised

Table 1. Effect of process parameters on the formation rate of tin dispersion products, the pulse size ratio j_a:j_c = 1:1.

Electrolyte	pH	j_{av}, A·cm^{-2}	Potential of pause, V vs. Ag/AgCl		Formation rate, mg·(cm^{-2}·h^{-1})
			After anodic pulse	After cathodic pulse	
1 mol·L^{-1} NaOH	14,0	1.00	−0.20	−0.53	—
1 mol·L^{-1} NaF	8,6	0.10	−0.20	−0.51	4.5±0.5
		0.50			10.2±0.9
		0,75			28.0±2.0
		1.00			56.5±3.0
1 mol·L^{-1} NaCl	7,0	0.10	−0.22	−0.50	14.7±1.0
		0.50	−0.22	−0.50	23.5±2.3
		0.75	−0.22	−0.50	130.7±4.5
		1.00	−0.22	−0.50	180.3±6.3

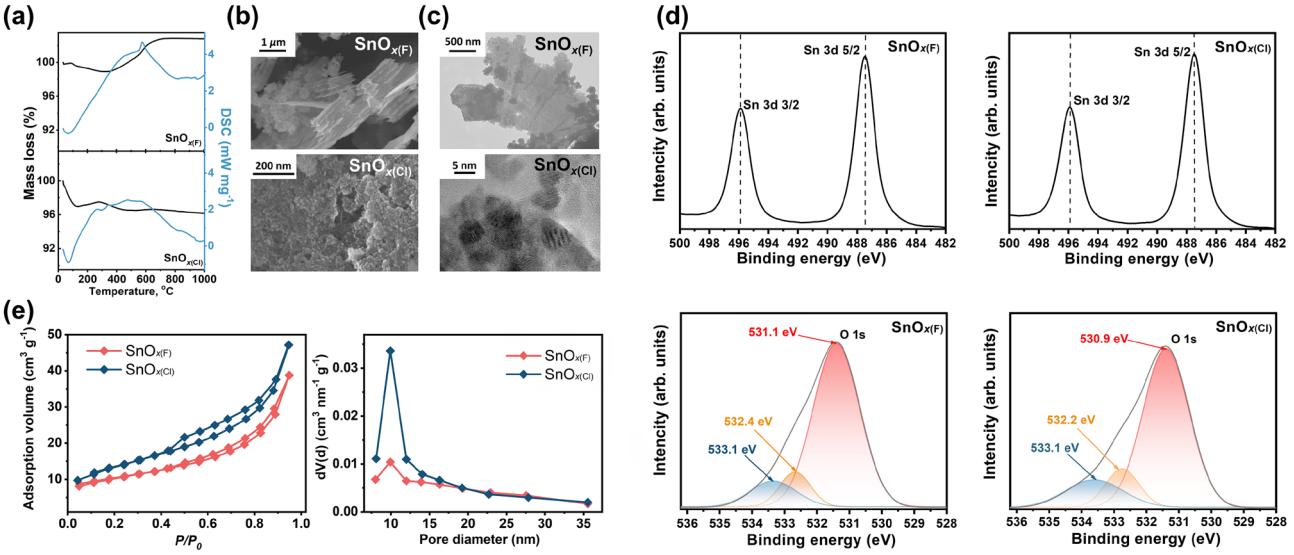

Fig. 2. TGA/DSC analysis curves of SnO_x materials prepared via pulse electrolysis, 10 K·min^{-1}, air atmosphere (a). SEM (b) and TEM (c) images of SnO_x-based materials. XPS spectra of $SnO_{x(F)}$ and $SnO_{x(Cl)}$ samples at Sn3d and O1s regions (d). N_2 adsorption isotherms and pore size distributions of $SnO_{x(F)}$ and $SnO_{x(Cl)}$ samples (e).

by an initial decrease in sample mass of 1.12% as a result of the removal of structural water and a further increase in mass of 3.93% due to the pre-oxidation of non-stoichiometric initial products, SnO and Sn phases, to SnO_2. In contrast, the SnO_x material synthesised in a NaCl electrolyte did not exhibit an increase in mass, indicating the absence of a significant quantity of non-stoichiometric products and lower tin oxides or metallic tin in the composition of the material. This finding aligns with the XRD data.

According to the SEM and TEM data (Fig. 2b, c), tin oxides obtained in a NaF electrolyte and having heterogeneous composition according to XRD were characterised by strongly anisotropic shape and particle size. As can be observed, the $SnO_{x(F)}$ material comprised two distinct phases: nanometre-sized spherical particles and micrometre-sized flake-like structures. In contrast, the SnO_x synthesized in a NaCl electrolyte ($SnO_{x(Cl)}$) exhibited a homogeneous structure, comprising spherical particles of approximately 6–8 nm, which were combined into micrometer-sized agglomerates.

The results of the XPS analysis (Figure S2) showed that the change in the anion of the electrolyte had no effect on the shape of the three-component O1s line, and single-component lines of the Sn3d 5/2 and Sn3d 3/2 (Fig. 2d). The binding energy value of Sn 3d 5/2 ranged from 487.0 to 487.2 eV, and that of Sn 3d 3/2 was within 495.4–495.6 eV. The O1s line in all samples had three components with binding energies in the range of 530.9–533.1 eV, which could refer to Sn-O-Sn (530.9–531.1 eV), Sn = O (532.2–532.4 eV) and adsorbed water (533.1 eV) [46, 47].

The $SnO_{x(F)}$ and $SnO_{x(Cl)}$ samples demonstrated the typical IV-type isotherm with a H_4-type hysteresis [48]. The S_{BET} values for the $SnO_{x(F)}$ and $SnO_{x(Cl)}$ samples were 35 and 47 m^2·g^{-1}, respectively, which coincides with a difference in particle sizes evaluated via XRD, and the pore volumes of –0,384 and 0,538 cm^3·g^{-1} for $SnO_{x(Cl)}$ and $SnO_{x(F)}$, respectively. The decline in the hysteresis loop and the decrease in S_{BET} of $SnO_{x(Cl)}$ are likely owing to the presence of particles with broad size distributions and anisotropic shapes.

Thus, by varying such technological parameters as the anionic composition of the electrolyte, pulse electrolysis enables the production of dispersed non-hydrated tin oxides with controlled composition and microstructural characteristics, with no use of capping agents and no necessity for high-temperature post-treatments.

3.2. A comparative study of the functional properties of tin oxide-based materials

3.2.1. LIBs performance

Tin-containing materials are a promising class of materials with the requisite characteristics (widespread availability, relatively low cost, and high theoretical capacity) for use as anode materials in LIBs [49].

The reduction processes of both SnO and SnO_2 in the presence of Li ions are a two-step reaction involving the initial reduction of tin oxides to Sn:

$$SnO_2 + 4Li^+ + 4e^- \rightleftarrows 4Sn + 2Li_2O \quad (2)$$

$$SnO + 2Li^+ + 2e^- \rightleftarrows Sn + Li_2O \quad (3)$$

Subsequently, the resulting Sn phase is fused with Li ions:

$$Sn + xLi^+ + xe^- \rightleftarrows 4Li_xSn\left(0 \le x \le 4.4\right) \quad (4)$$

A galvanostatic study of Sn-containing materials prepared under pulse electrolysis conditions in NaCl and NaF electrolytes ($SnO_{x(Cl)}$ and $SnO_{x(F)}$, respectively) demonstrated that the anode material based on $SnO_{x(Cl)}$, whose main phase was SnO_2, exhibited favourable charge-discharge characteristics at varying charge-discharge rates (from C/20 to 2C). The reversible capacity in C/20 mode was found to be 680 mAh·g^{-1}, which is in close proximity to the theoretical value of the SnO_2 capacity (790 mAh·g^{-1}). The reversible capacity in 2C mode was approximately 440 mAh·g^{-1}. Upon recycling the material at a charge-discharge rate of C/20 following 2C, the capacity was observed to be 620 mAhg^{-1} (Fig. 3a) [50].

The anode material based on $SnO_{x(F)}$, whose main phase was SnO, exhibited inferior charge-discharge characteristics in comparison to $SnO_{x(Cl)}$ (Fig. 3a). The reversible capacity at a charge-discharge rate of C/20 was 509 mAh·g^{-1} whereas in 2C mode it was approximately 382 mAh·g^{-1}. Upon recycling in C/20 mode after 2C, the $SnO_{x(F)}$ material exhibited a capacity of only 370 mAh·g^{-1}, failing to revert to its initial C/20 capacity value observed for the $SnO_{x(Cl)}$ material (Fig. 3a). It is noteworthy that for both $SnO_{x(Cl)}$ and $SnO_{x(F)}$ materials, capacitance values exceeding the theoretical ones (1475 mAh·g^{-1} and 1334 mAh·g^{-1} for $SnO_{x(Cl)}$ and $SnO_{x(F)}$, respectively) were observed during the initial charge cycle. These values include irreversible capacitances resulting from the formation of solid electrolyte interface (SEI).

The repeated electrochemical cycling of tin oxide-based materials has been observed to result in a progressive degradation of the Li_2O matrix, which in turn leads to a decrease in anode capacitance. Nanoscale electroactive tin-containing materials ($SnO_{x(Cl)}$) provide sufficient free space to absorb the stress generated during the lithiation/delithiation process, a large active surface area and a reduced Li^+ diffusion length [49], while the dense SnO film structure in $SnO_{x(F)}$ acts as a diffusion barrier [51]. It can be reasonably deduced that the disparate electrochemical properties observed in these materials when employed as LIBs anode materials can be attributed to the morphological dissimilarities between $SnO_{x(Cl)}$ and $SnO_{x(F)}$ (Fig. 2b, c).

3.2.2. Photocatalysis properties

One of the principal areas of research within the field of ecological catalysis is heterogeneous photocatalysis, which is focused on the purification of water resources from a range of organic pollutants [52]. A variety of semiconductor materials, including metal oxides, have been demonstrated to possess favorable photocatalytic properties, which can be employed in water purification processes to effectively remove contaminants from water [53].

Only a limited number of papers have reported that SnO_2-SnO catalytic systems resulted in an increased rate of photocatalytic dye decomposition in comparison to pure SnO_2; this could be achieved by inhibiting the electron-hole recombination process [54, 55].

Fig. 3b illustrates the alteration in the absorption spectrum of MB upon photodegradation in the presence of SnO_x-based materials obtained through pulse electrolysis. As the potential of SnO_2 nanoparticles for photocatalytic water purification has been the subject of several studies [56, 57], a utilization of SnO or SnO_2-SnO materials as a photocatalyst is less prevalent in scientific publication than the utilization of SnO_2. As the irradiation time is increased, the intensities of the bands at 664 and 612 nm diminish rapidly, and the solution undergoes a change in coloration. This phenomenon indicates the processes of adsorption/photodegradation of MB, which are caused by the destruction of the sulfur-nitrogen system in the MB molecule. Furthermore, the UV-vis spectra exhibit a shift of two bands with increasing irradiation time, which may be attributed to the demethylation of MB molecules and their conversion to other intermediates [58].

It is important to note that the initial stage of the UV irradiation process was preceded by a period designated as the dark phase. The duration of the dark phase was determined through experimentation to be 30 minutes, at which point the intensity of the MB absorption spectrum ceased to undergo further change.

In Fig. 3c, the preceding dark phase, designated as "Dark", is conventionally positioned on the negative portion of the abscissa axis. The photodegradation process itself should occur within the "UV" mode. The photodegradation rate (C/C_0), defined as the ratio of the MB concentration at a specified time point (C) to the initial MB concentration (C_0), was calculated from the maximum MB absorbance (the inset in Fig. 3b) as a function of time. It was demonstrated that the concentration of MB decreased by over 90% following UV-vis irradiation for 30 minutes when both $SnO_{x(Cl)}$ and $SnO_{x(F)}$ materials were employed. However, in the subsequent dark phase, an increase in the concentration of MB in the solution in which the $SnO_{x(Cl)}$ material was used was observed, reaching

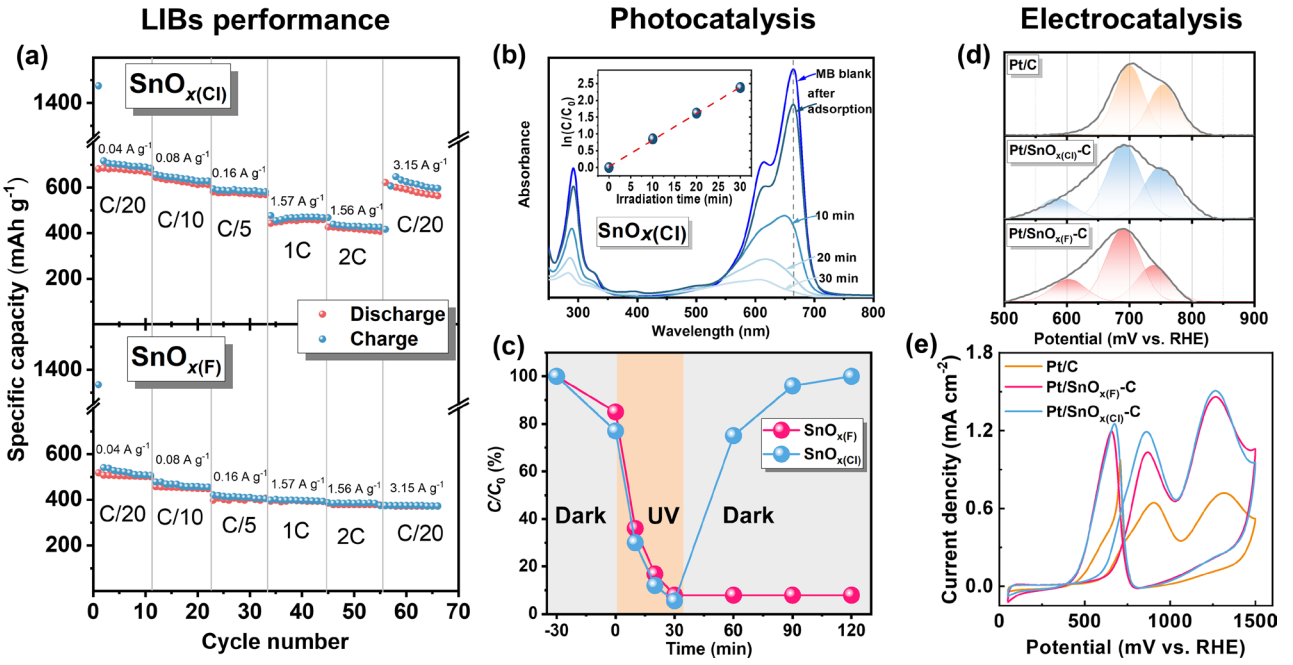

Fig. 3. Specific capacitances of $SnO_{x(Cl)}$ and $SnO_{x(F)}$ materials as a function of cycle number and charge/discharge rate (a). Time-dependent UV-vis absorption spectra of MB, the concentration of MB = 10 ppm, λ = 365 nm, the inset – pseudo-first order kinetics plot for the MB degradation process using the $SnO_{x(F)}$ material (b). Dependence of MB concentration changes on adsorption time and UV irradiation (c). Decomposition of the multicomponent CO-stripping peaks of Pt/C and Pt/SnO_x-C materials (d). CV curves of Pt/C and Pt/SnO_x-C materials in 0.5 mol·L^{-1} C_2H_5OH + 0.5 mol·L^{-1} H_2SO_4 electrolyte, scan rate 50 mV·s^{-1} (e).

96% after 90 minutes. This finding suggests that the $SnO_{x(Cl)}$ material did not exhibit photocatalytic properties, but rather demonstrated adsorption characteristics. In contrast, the $SnO_{x(F)}$ material displayed a distinct lack of such behavior (Fig. 3c), with the photodegradation of MB occurring almost entirely.

The decomposition of MB under UV-vis irradiation using the $SnO_{x(F)}$ material is in accordance with the pseudo-first order kinetic model. Inset in Fig. 3b illustrates the relationship between the $\ln(C_0/C)$ ratio and irradiation time. The pseudo-first order rate constant (k) can be estimated from the slope of the linear plot. The plot of the data demonstrates a strong linear correlation, with a correlation coefficient (R^2) value approaching 1. The calculated rate constant value was 0.0791 min^{-1} [33], which exceeds the k values for tin oxide-based materials obtained by alternative laboratory methods. This may be attributed to the inhibition of the photogenerated electron-hole recombination process, which is facilitated by effective charge separation in the SnO_2-SnO semiconductor system.

3.2.3. *Electrocatalysis properties*

The development of low-temperature fuel cell technology has attracted considerable attention, with researches focusing on not only hydrogen fuel cells but also fuel cells utilising the direct oxidation of liquid fuels. The investigation of methanol as a potential fuel has attracted considerable attention within the scientific community [59–61]. Nonetheless, the toxicological attributes of methanol represent a significant impediment to the deployment of methanol in operational energy systems based on fuel cells. From this perspective, ethanol is a more promising fuel for low-temperature fuel cells [62, 63], which can be produced in large quantities through biomass fermentation processes [64].

The electrochemical oxidation of ethanol in an acidic aqueous solution can proceed via the formations of $C1_{ads}$ and $C2_{ads}$ stable intermediates, which subsequently yield CO_2 (hereinafter, $C1_{ads}$ will be denoted as CO) [65–70]:

$$CH_3CH_2OH \rightarrow [CH_3CH_2OH]_{ads} \rightarrow Cl_{ads}, C2_{ads} \rightarrow CO_2 \quad (5)$$

Secondly, it can be oxidised to formic acid:

$$CH_3CH_2OH \rightarrow [CH_3CH_2OH]_{ads} \rightarrow CH_3CHO \rightarrow CH_3COOH \quad (6)$$

It is well established that tin acts as an effective promoter for the electrochemical oxidation of ethanol on Pt-containing catalysts. This is attributed to the greater oxyphilic nature of tin and its oxides compared to other members of the Pt group metals [71].

When tin is present in the catalytic system, ethanol oxidation proceeds by a bifunctional mechanism [72], which can be broken down into the following three stages:

(i) the adsorption of organic species on Pt:

$$Pt + CO \rightarrow Pt - CO_{ads} \quad (7)$$

(ii) the adsorption of oxygen-containing species on the tin component, which itself can act as a source of oxygen-containing species:

$$Sn + H_2O \rightarrow Sn - OH_{ads} + H^+ + e^- \quad (8)$$

(iii) the chemical interaction between the organic species and oxygen-containing species.

$$Pt - CO_{ads} + Sn - OH_{ads} \rightarrow CO_2 + H^+ + e^- \quad (9)$$

It has been previously demonstrated [73] that the composition and microstructural characteristics of the carrier have no impact on the size and crystallographic properties of Pt nanoparticles obtained under pulse electrolysis conditions. This may be attributed to the fact that the formation of Pt nanoparticles, when an alternating pulse current is applied to Pt electrodes, does not occur through the dissolution of Pt. Instead, it is the result of the introduction of alkali metal cations into the Pt crystal lattice, the formation of an intermetallic compound of Pt and alkali metal, and the decomposition of the intermetallide, accompanied by the mechanical breaking of the loosened surface of the Pt electrode [18, 44].

The aforementioned advantage of pulse electrolysis permitted an exact evaluation of the influence of the composition and properties of the tin component, while the microstructural characteristics of the Pt component were preserved.

The preliminary investigation of Pt/SnO_x-C catalysts was conducted through CO-stripping, a method that enables the assessment of the electrochemically active surface area of the catalyst (Figure S3, Table S2), a crucial attribute of Pt-containing electrocatalytic systems. Additionally, this approach allows for the evaluation of the catalyst's tolerance to $C1_{ads}$ intermediates.

Fig. 3d illustrates the decomposition of the multicomponent peaks associated with CO electrooxidation over Pt/C and Pt/SnO_x-C catalysts. In the case of Pt/C material, the CO oxidation peak exhibits two subpeaks at potentials of 700 mV and 760 mV. In the case of Pt/SnO_x-C catalysts comprising a single catalytically active phase (in this instance, Pt), the observation of discernible CO oxidation at differing potential values may be attributed to the bifunctional mechanism of CO oxidation, particularly in relation to structural effects. These encompass the varying adsorption energies of oxygen-containing species and CO-type species on Pt. Moreover, the peak splitting observed in CO stripping voltammogram on Pt/C catalysts occurs due to CO oxidation on Pt nanoparticles agglomerates as well as individual Pt nanoparticles. In contrast to Pt/C, both Pt/$SnO_{x(Cl)}$-C and Pt/$SnO_{x(F)}$-C are distinguished by the presence of an CO oxidation pre-peak at significantly more cathodic potentials, which is observed to a considerable extent at 600 mV (Fig. 3d). The incorporation of SnO_x into the catalyst support composition has the potential to significantly diminish the overvoltage associated with the electrochemical CO oxidation process (or $C1_{ads}$ intermediates). This, in turn, results in an increase in the rate of ethanol oxidation on SnO_x-containing catalysts (Fig. 3d). The cyclic voltammograms (CVs) of the investigated Pt/C and Pt/SnO_x exhibit a typical shape for Pt-containing materials (Fig. 3e). The CVs are characterised by ethanol oxidation peaks in the potential ranges of 600–1000 mV and 800–400 mV on the anodic and cathodic courses, respectively. In general, all tin-containing materials (Pt/SnO_x-C) exhibited a notable reduction in both the ethanol oxidation onset potential (E_{onset}) and the ethanol oxidation peak potential (E_{peak}) in comparison to the tin-free materials (Pt/C). (Figure S3, Table S2). The highest electrocatalytic activity, as indicated by the rate of ethanol oxidation at a potential of 0.6 V ($j_{0.6V}$) and at oxidation peak potentials (j_{peak}), was demonstrated by the Pt/$SnO_{x(Cl)}$-C material. This material is characterised by the predominance of the tin component in its composition in the form of SnO_2 (Table S1) and the isotropic shape of SnO_2 particles (Fig. 2b, c). The Pt/$SnO_{x(F)}$-C material, which is predominantly composed of tin in the form of SnO (Table S1) and exhibits anisotropic particle shape (Fig. 2b, c), demonstrated nearly identical overvoltage values for the ethanol oxidation process (Fig. 3e), yet exhibited a comparatively lower rate of ethanol oxidation in comparison to the Pt/$SnO_{x(Cl)}$-C material.

3.3. Principles of SnO_x design and synthesis using pulse alternating current conditions

It is established that tin is among the metals that readily undergo oxidation to form dispersed oxide forms when subjected to anodic polarization conditions [74]. In acidic electrolytes, tin is observed to undergo a dissolution, forming Sn^{2+} and Sn^{4+} ions. Conversely, in alkaline electrolytes, tin is known to form stannates and stannites [75]. In this context, electrolytes with pH values proximate to neutrality are optimal for the production of dispersed tin oxides under pulse electrolysis conditions.

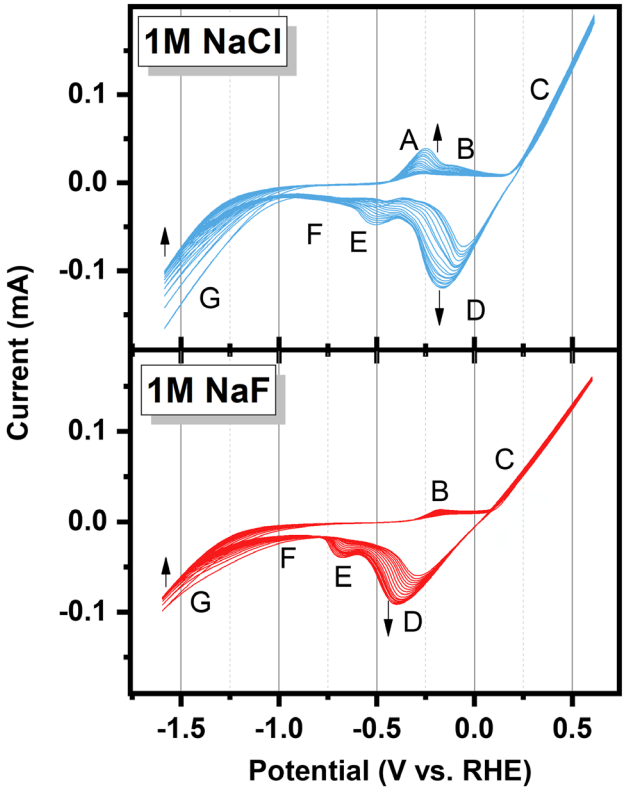

Fig. 4. Multiple cycling curves of Sn electrode in 1 mol·L⁻¹ NaCl and 1 mol·L⁻¹ NaF solutions, potential sweep rate 50 mV·s⁻¹.

The electrochemical behaviour of tin has been previously investigated in solutions with different pH values (and relatively low concentrations of 0.01–0.10 mol·L^{-1}), including borate buffer [74, 76, 77], bicarbonate buffer [78] and dilute aqueous NaOH solution in the presence of halide ions [79].

The CV curves of the tin electrode in 1 mol·L^{-1} NaCl and 1 mol·L^{-1} NaF electrolytes were obtained over a wide range of potentials (Fig. 4). In 1 mol·L^{-1} NaCl, the anodic course of the CV curve (Fig. 4) exhibited a peak (A) at a potential of –0.25 V vs. RHE and a subsequent shoulder (B) at a potential of the order of –0.14 V vs. RHE, which can be attributed to the formation of different tin oxide forms. An additional increase in potential within the anodic region (E > 0.0 V) was observed to be characterised by a monotonic increase in current density (C), which may be attributed to the formation of a passive film on the surface of the tin electrode. Two pronounced peaks were observed at potentials of –0.17 V (D) and –0.52 V (E), as well as in region F at –0.8 V, on the cathodic course of the CV curve. These peaks were caused by the reduction of tin oxide forms that had been formed during the anodic sweep of the potential. A further sweep of the potential into the cathode region reveals an increase in cathode current density (at E < –1.1 V vs. RHE), which can be attributed to the electrochemical hydrogen evolution process. It is important to note that the SnO_x film formed on the tin surface is not fully reduced, and the release of hydrogen can contribute to the mechanical removal of tin oxides from the surface of the tin electrode.

A comparable picture was observed in 1 mol·L^{-1} NaF electrolyte (Fig. 4), with the exception that Peak A was not identified on the anodic course of the CV curve, and Peaks D and E on the cathodic course of the curve were shifted to the cathodic side. This can be attributed to the challenge of reducing tin oxide forms that are generated on the anodic course of the CV, due to the varying pH values of the electrolytes and the distinct mechanisms of interaction between Cl^- and F^- ions with the Sn surface. These factors will be elaborated upon subsequently.

The optimal formation rate of products resulting from the electrochemical oxidation/destruction of tin electrodes (1.0 A·cm^{-2}) was observed in both Cl^- and F^- containing electrolytes. These results were attributed to temperature-dependent processes occurring in the near-electrode region, where an increase in average pulse current density (j_{av}) led to a notable change in temperature. This phenomenon was evident in both electrolytes, with the temperature of the near-electrode layer remaining relatively constant upon reaching j_{av} = 1.0 A·cm^{-2} (Fig. 5a).

The correlation among the accumulation rate of dispersion products, temperature effect (Fig. 5a) and the average density of alternating pulsed current may be attributed to the fact that under conditions of pulsed electrolysis, there is a limiting degree of filling of the electrode surface, which consequently leads to the formation of gas bubbles in the near-electrode region.

The application of an alternating pulse current with an average density of 1.0 A·cm^{-2} to Sn electrodes (Fig. 5b) in the absence of stirring results in the measurement of a temperature in the near-electrode layer exceeding 130–140 °C. Upon stirring and cooling the electrolyte, a decrease in temperature was observed, reaching a stable velocity of 0.314 m·s^{-1} at approximately ~110 °C. Concurrently, the temperature of the electrolyte solution during the stirring process was consistently maintained at a range of 40–50 °C. The temperature effects observed in the boundary layer indicate the potential for in situ dehydration of the Sn oxide products formed under pulse electrolysis conditions. This is supported by the absence of chemically bound water, as confirmed by the XRD phase information (Figure S1, Table S1) and thermogravimetric (Fig. 2a) analysis results. It is important to note that the thickness of the stationary electrolyte layer in proximity to the electrode is dependent on the linear

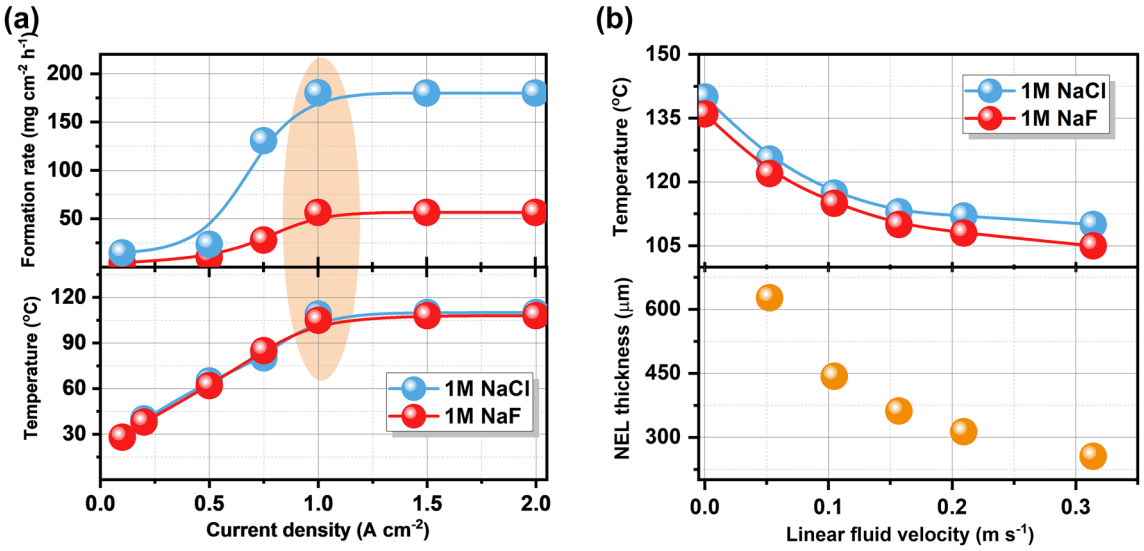

Fig. 5. Dependence of the formation rate of dispersed SnO_x products under pulse electrolysis conditions on electrode material, electrolyte and average density of alternating pulse current, and dependence of near-electrode layer temperature on average density of alternating pulse current, electrode material and electrolyte, linear fluid velocity 0.314 m·s^{-1} (a). Dependence of the near-electrode layer temperature of Sn electrodes on the linear fluid velocity of the electrolyte at j_{av} = 1.0 A·cm^{-2}, yellow balls – estimated value of the near-electrode layer thickness as a function of linear fluid velocity of the electrolyte (b).

velocity of the liquid, reaching a maximum value of 0.314 m·s^{-1} (Fig. 5b). Despite the forced mixing of the electrolyte, which results in thermal (or thermokinetic) effects at the electrode-electrolyte boundary, this value is not exceeded.

It has been demonstrated that the application of an alternating pulse current to Sn electrodes in an aqueous electrolyte containing Cl^- or F^- halogen ions results in the formation of dispersed SnO_x products of varying composition and microstructure. The material obtained in a NaCl electrolyte was found to be a mixture of SnO and SnO_2 phases, with the former representing 3% and the latter 97% of the total composition. The particles exhibited an isotropic structure and a mean diameter of 7.6 nm, as determined by XRD analysis. The material obtained in a NaF electrolyte was also a mixed phase, with the highest concentrations observed for SnO (85%) and SnO_2 (12%). Furthermore, the material obtained by dispersing in a NaF electrolyte included a mixed phase of metallic tin and $Sn_6O_4(OH)_4$, with a maximum content of 2%. In contrast, the particles structure of this material was markedly anisotropic, with two distinct phases discernible: micrometre-scale plate-like particles and nanometre-sized agglomerates of spherical particles (Fig. 2b, c).

Firstly, in order to elucidate the considerable impacts of electrolyte anion on the composition and structure of tin-containing materials obtained under pulse electrolysis conditions, it is essential to highlight the discrepancy in pH between the two electrolytes employed: pH(NaCl) = 7.0, pH(NaF) = 8.6. This discrepancy is typically attributed to the capacity of the NaF anion to react with water, resulting in the formation of the OH^- and weak hydrofluoric acid HF:

$$NaF + H_2O \rightarrow Na^+ + OH^- + HF \quad (10)$$

In contrast, NaCl is a salt formed by the strong acid HC1, which dissociates completely in water, thereby maintaining a neutral pH in the electrolyte.

The observed differences can be attributed to the nature of the anion, specifically its ability to interact with solutes in a kosmotropic or chaotropic manner [80]. The formation of ion pairs in aqueous solutions containing halogen compounds is governed by the law of matching water affinities (LMWA), as postulated by Collins [81, 82]: ions with opposite charges and the same affinity for water (known as kosmotropes) tend to form contact ion pairs, whereas ions with opposite charges and different affinities for water (chaotropes) remain in their respective hydrate shells. When a kosmotropic ion interacts with an oppositely charged chaotropic ion, the attraction of the chaotropic ion is insufficient to cause the kosmotropic ion to lose its hydrate shell. Consequently, the kosmotrope/chaotrope pair is invariably separated by water and is unable to form strong ion pairs [81]. The behaviour of HF as a weak acid is explained by the positive pK value [83], which is the result of the strong interaction between H^+ and F^-. This interaction

prevents HF from dissociating completely in water, as H^+ is a kosmotropic cation [81]. In contrast, the corresponding acids of other chaotropic halides, including HCl, are strong acids, with large negative pK values [83] due to their greater affinity for H^+.

In consideration of the kosmotropic/chaotropic characteristics of the electrolyte anion, a series of potential processes that may occur at the Sn electrode under pulsed electrolysis conditions in halogen-containing electrolytes can be postulated.

The formation of diverse oxide forms on the surface of the Sn electrode and its passivation occurs within a sufficiently broad potential range, a conclusion that was corroborated by voltammetric studies (Fig. 4). During the anodic pulse, the oxidation on the Sn electrode occurs with the formation of doubly charged Sn ions. The charge of these particles is always +2, regardless of the type of anion (F^- or Cl^-) and the pH of the electrolyte [80]:

$$Sn \rightarrow Sn^{2+} + 2e^- \tag{11}$$

Concurrently, the formation of hydrated Sn oxides occurs:

$$Sn + 2OH^- \leftrightarrow Sn(OH)_2 \tag{12}$$

As the electrode potential increases, the formation of a passive film occurs, resulting in the formation of a stable $Sn(OH)_4$ compound.

$$Sn(OH)_2 + 2OH^- \rightarrow Sn(OH)_4 \tag{13}$$

The anodic pulse at the electrode can reach high values of current density, which may result in competing processes of oxygen, and chlorine and hypochlorite ions evolution:

$$4OH^- \rightarrow O_2 \uparrow + 2H_2O + 4e^- \tag{14}$$

$$Cl^- \rightarrow Cl_2 \uparrow + 2e^- \tag{15}$$

$$Cl^- + 2OH^- \leftrightarrow ClO^- + 2H_2O + Cl^- \tag{16}$$

Additionally, the ClO^- anion presented in the anodic half-period can undergo conversion to a metastable ClO_3^- anion, which subsequently transforms into a stable ClO_4^- anion.

Nevertheless, all these anions are distinguished by the lowest specific adsorption on metals, metal oxides among other inorganic ions [87]. Consequently, they are unlikely to exert a substantial influence on the morphology of the products formed under pulse electrolysis conditions.

During the interval following the anodic pulse, the $Sn(OH)_2$ and $Sn(OH)_4$ compounds undergo dehydration, resulting in the formation of oxides phase:

$$Sn(OH)_2 \rightarrow SnO + H_2O \tag{17}$$

$$Sn(OH)_4 \rightarrow SnO_2 + 2H_2O \tag{18}$$

During the cathodic pulse, irrespective of the nature of the anion, hydrogen release reactions occur at the Sn electrode, resulting in the accumulation of OH^- in the near-electrode region and, furthermore, providing passivation processes for the Sn electrode surface:

$$2H_2O + 2e^- \rightarrow H_2 \uparrow + 2OH^- \tag{19}$$

The rapid release of hydrogen facilitates the destruction of the oxide film and the dispersion of the resulting Sn oxides into the electrolyte.

A period of pause ensues following the cathode pulse at the potential E = –0.5 V vs. Ag/AgCl, during which the following processes may occur:

$$Sn(OH)_2 + 2OH^- \leftrightarrow \left[Sn(OH)_3\right]^- \tag{20}$$

$$n\left[Sn(OH)_3\right]^- \leftrightarrow n SnO \cdot n H_2O_{(s)} \tag{21}$$

It should be noted that the $Sn_6O_4(OH)_4$, which was identified in the material obtained by oxidation/destruction Sn electrodes under pulse electrolysis conditions in a NaF electrolyte, is a crystalline form of hydrated oxide. This phase was formed according to Eq. (21) and is present in an amount of approximately 1%. It is a stable phase that undergoes dehydrogenation to form $6SnO{\cdot}2H_2O$ even at room temperature [84]:

$$Sn_6O_4(OH)_4 \rightarrow 6SnO + 2H_2O \tag{22}$$

It can be reasonably deduced that the formation of Sn oxides on the surface of the Sn electrode is dependent on the alkalinisation of the near-electrode layer (Eq. (16)), regardless of the type of electrolyte anion. The type of electrolyte anion is the sole determining factor in the microstructure of the formed Sn oxides. When hydrated kosmotropic F^- anions are adsorbed on the surface of the passive film on the Sn electrode, they tend to not lose their hydrate shell. This is due to the relatively high activation energy of the process, which prevents the shell from being broken down. The fluoride anions have the capacity to partially dehydrate and interact with the surface Sn cations

presented in the passive film, which also exhibit a sufficiently high surface charge density in accordance with the LMWA [80–82], resulting in the formation of tin fluoride complexes:

$$Sn^{2+} + nF^{-} \rightarrow [SnF_n]^{2-} \quad (23)$$

which can undergo further transformation into SnO and SnO_2 phases.

It is important to note that, due to the F^- ion having the smallest ionic radius (0.133 nm) [85] among all halogen ions and the highest electronegativity among halogens on the Pauling scale [86], the stability constant of tin fluoride complexes is 2.5–5 times greater than that of tin chloride complexes having similar composition [88]. It can, therefore, be concluded that only the F^- anion is capable of forming stable complexes with Sn. Nevertheless, the kosmotropic nature of the F^- anion is insufficient for rapid penetration of the passive surface layer on the Sn electrode. As an alternating pulse current is applied to the Sn electrode, defects and cracks are formed within the passive film, leading to the destruction of the passive layer. This results in the microstructure of the Sn-containing material obtained under pulse electrolysis conditions utilising a NaF electrolyte and exhibiting micrometre-sized plate-shaped particles (Fig. 2b, c). This fact gives rise firstly to the presence in this material of an additional Sn-containing phase with fundamentally different microstructural characteristics (Fig. 2b, c) and secondly to the observation that the kinetics of the Sn-containing material formation in a NaF electrolyte is slower than that in a NaCl electrolyte (Fig. 5a).

The adsorption of chaotropic Cl^- anions on the surface of the passive film on the Sn electrode does not result in the formation of corresponding Sn complexes [80]. Nevertheless, due to the ease with which Cl^- anions can shed their hydrate shell, they demonstrate a superior capacity to penetrate the passive layer in comparison to kosmotropic F^- anions. This can result in a localised weakening of the film structure, thereby facilitating the penetration of the electrolyte solution into the passive layer and enabling direct contact with the underlying Sn surface.

It can be concluded that, irrespective of the type of electrolyte anion, a passive oxide film is invariably formed on the surface of the Sn electrode when a pulse electrolysis is employed. The kinetics of the formation process of Sn-containing material (Fig. 5a), its microstructural characteristics and composition are contingent upon the kosmotropic/chaotropic nature of the electrolyte anion. In this instance, the utilisation of an alternating pulse current, which facilitates the process of hydrogen evolution during the cathode pulse, determines the feasibility of obtaining dispersed Sn oxides.

4. Conclusions

The Sn electrochemical behaviour under pulsed electrolysis conditions utilising an alternating pulsed current was dependent upon the current density, pH and anionic composition of the electrolyte. Attaining high anodic potentials at the instant of anodic pulse generation would ensure the formation of an oxide phase on the surface of the Sn electrode. The formation rate of Sn oxides was found to be increased in proportion to the average current density.

In the context of pulse electrolysis in electrolytes containing Cl^- or F^- anions, the oxidation/destruction of Sn electrode led to the formation of dispersed Sn oxides. The composition and microstructural characteristics of these oxides were contingent upon the differing stability of the Sn fluoride and chloride complexes, as well as the distinct mechanisms of interaction between Cl^- and F^- anions with the oxidised Sn surface, which are influenced by the varying kosmotropic/chaotropic nature of these anions. The composition and microstructural characteristics of Sn oxides obtained under pulse electrolysis conditions determined their potential applications as an anode material for lithium-ion batteries, photocatalysts, or as part of Pt-containing electrocatalytic systems.

The utilisations of aqueous electrolytes and elevated true current densities during pulse moments may result in consistent alteration processes of oxygen and hydrogen releases, including those that lead to the disordering of the surface oxidised layer on the Sn electrode. This would facilitate the penetration of electrolyte components and gaseous products into the layer structure, thereby promoting the mechanical dispersion of oxidised Sn. The presence of halogen anions in the electrolyte would facilitate complexation processes during the anodic pulse. The difference in the dissociation mechanisms of the electrolyte with different halogens in water could determine the composition and microstructural characteristics of the formed dispersed products.

The limited duration of the current pulse allowed the complexation process and oxide film growth on the Sn surface to be limited in time. Furthermore, the presence of a pause made the concentration restrictions on halogen anions in the near-electrode layer to be removed, thus preventing Sn passivation as a result of increasing pH in the near-electrode layer. The combination of a semiconducting oxide film and a high gas filling of the electrolyte in the near-electrode layer resulted in high ohmic losses, which in turn caused local superheats at the interface. This

phenomenon contributed to the *in situ* dehydration of the formed products of Sn dispersion under conditions of pulse electrolysis.

Consequently, by modifying the anionic composition of the electrolyte, a pulse electrolysis as an electrochemical top-down approach enables the production of dispersed non-hydrated Sn oxides with precisely defined composition and microstructural attributes, eliminating the necessity for capping agents and circumventing the need for high-temperature post-treatments. The composition and microstructural characteristics of SnO_x materials can be varied in order to tailor their functional affiliation to electrochemical and photocatalytic applications.

Supporting Information

Supporting information for this article is available at https://jelectrochem.xmu.edu.cn/journal/

Acknowledgements

This work was supported by the Ministry of Science and Higher Education of the Russian Federation under Project FENN-2024-0002.

Conflict of interest

The authors declare no competing interest.

Data availability

Data will be made available on request.

References

[1] Terna A D, Elemike E E, Mbonu J I, Osafile O E, Ezeani R O. The future of semiconductors nanoparticles: synthesis, properties and applications[J]. Mater. Sci. Eng. B, 2021, 272: 115363.

[2] Hossain N, Mobarak M H, Mimona M A, Islam M A, Hossain A, Zohura F T, Chowdhury M A. Advances and significances of nanoparticles in semiconductor applications – A review[J]. Results in Engineering, 2023, 19: 101347.

[3] Mishra S R, Ahmaruzzaman M. Tin oxide based nanostructured materials: synthesis and potential applications[J]. Nanoscale, 2022, 14(5): 1566–1605.

[4] Yang Y, Guo L P, Wang X P, Li Z Z, Zhou W. Halogen modified organic porous semiconductors in photocatalysis: mechanism, synthesis, and application[J]. Adv. Powder Mater., 2024, 3(2): 100178.

[5] Shabna S, Dhas S S J, Biju C S. Potential progress in SnO_2 nanostructures for enhancing photocatalytic degradation of organic pollutants[J]. Catal. Commun., 2023, 177: 106642.

[6] Lan X X, Xiong X Y, Liu J, Yuan B, Hu R Z, Zhu M. Insight into reversible conversion reactions in SnO_2-based anodes for lithium storage: a review[J]. Small, 2022, 18(26): 2201110.

[7] Ansari M Z, Ansari S A, Kim S H. Fundamentals and recent progress of Sn-based electrode materials for supercapacitors: a comprehensive review[J]. J. Energy Storage, 2022, 53: 105187.

[8] Chisaka M. Review of carbon-support-free platinum and non-platinum catalysts for polymer electrolyte fuel cells: will they feature in future vehicles?[J]. J. Mater. Chem. A, 2024, 12: 18615–19582

[9] Sun C Y, Yang J K, Xu M, Cui Y, Ren W W, Zhang J X, Zhao H L, Liang B. Recent intensification strategies of SnO_2-based photocatalysts: a review[J].Chem. Eng. J., 2022, 427: 131564.

[10] Han J H, Teng X Y, Jia W H, Liu P, Li Y M, Wang W D. SnO_2/Fe_2O_3/Cu_2O composites as catalysts for photoelectrocatalytic degradation of benzotriazoles[J]. Opt. Mater., 2024, 148: 114799.

[11] Inaba M, Murase R, Takeshita T, Yano K, Kosaka S, Takahashi N, Isomura N, Oh-ishi K, Yoshimune W, Tsuchiya K, Nobukawa T, Kodama K. Synthesis of a mesoporous SnO_2 catalyst support and the effect of its pore size on the performance of polymer electrolyte fuel cells[J]. ACS Appl. Mater. Interfaces, 2024, 16(8): 10295–19306.

[12] Guan M M, Zhao X R, Duan L B, Cao M M, Guo W R, Liu J R, Zhang W. Controlled synthesis of SnO_2 nanostructures with different morphologies and the influence on photocatalysis properties[J]. J. Appl. Phys., 2013, 114(11): 114302.

[13] Periyasamy M, Kar A. Modulating the properties of SnO_2 nanocrystals: morphological effects on structural, photoluminescence, photocatalytic, electrochemical and gas sensing properties[J]. J. Mater. Chem. C, 2020, 8(14): 4604–4635.

[14] Habte A G, Hone F G, Dejene F B. Effect of solution pH on structural, optical and morphological properties of SnO_2 nanoparticles[J]. Physica B Condens. Matter, 2020, 580: 411832.

[15] Sun X L. Morphosynthesis of SnO_2 nanocrystal networks as high-capacity anodes for lithium ion batteries[J]. Ionics, 2020, 26(8): 3841–3851.

[16] Wang H, Rogach A L. Hierarchical SnO_2 nanostructures: recent advances in design, synthesis, and applications[J]. Chem. Mater., 2014, 26(1): 123–133.

[17] Kuriganova A, Faddeev N, Gorshenkov M, Kuznetsov D, Leontyev I, Smirnova N. A comparison of "bottom-up" and "top-down" approaches to the synthesis of Pt/C electrocatalysts[J]. Processes, 2020, 8(8): 947.

[18] Leontyev I, Kuriganova A, Kudryavtsev Y, Dkhil B, Smirnova N. New life of a forgotten method: electrochemical route toward highly efficient Pt/C catalysts for low-temperature fuel cells[J]. Appl. Catal., A, 2012, 431: 120–125.

[19] Faddeev N A, Kuriganova A B, Leont'ev I N, Smirnova N V. Palladium-based electroactive materials for environmental catalysis[J]. Dokl. Phys. Chem., 2022, 507(1): 139–146.

[20] Kuriganova A B, Faddeev N A, Leontyev I N, Allix M, Rakhmatullin A, Smirnova N V. New electrochemical approach for the synthesis of Pd-PdO/C electrocatalyst and application to formic acid electrooxidation[J]. ChemistrySelect, 2019, 4(29): 8390–8393.

[21] Leontyeva D V, Leontyev I N, Avramenko M V, Yuzyuk Y I, Kukushkina Y A, Smirnova N V. Electrochemical dispergation as a simple and effective technique toward preparation of NiO based nanocomposite for supercapacitor application[J]. Electrochim. Acta, 2013, 114: 356–362.

[22] Chernysheva D, Vlaic C, Leontyev I, Pudova L, Ivanov S, Avramenko M, Allix M, Rakhmatullin A, Maslova O, Bund A, Smirnova N. Synthesis of Co_3O_4/CoOOH via electrochemical dispersion using a pulse alternating current method for lithium-ion batteries and supercapacitors[J]. Solid State Sci., 2018, 86: 53–59.

[23] Molodtsova T, Gorshenkov M, Kubrin S, Saraev A, Ulyankina A, Smirnova N. One-step access to bifunctional γ-Fe_2O_3/δ-FeOOH electrocatalyst for oxygen reduction reaction and acetaminophen sensing[J]. J. Taiwan Inst. Chem. Eng., 2022, 140: 104569.

[24] Molodtsova T, Gorshenkov M, Saliev A, Vanyushin V, Goncharov I, Smirnova N. One-step synthesis of γ-Fe_2O_3/Fe_3O_4 nanocomposite for sensitive electrochemical detection of hydrogen peroxide[J]. Electrochim. Acta, 2021, 370: 137723.

[25] Ulyankina A, Leontyev I, Maslova O, Allix M, Rakhmatullin A, Nevzorova N, Valeev R, Yalovega G, Smirnova N. Copper

oxides for energy storage application: novel pulse alternating current synthesis[J]. Mater. Sci. Semicond. Process, 2018, 731: 11–16.

[26] Ulyankina A, Leontyev I, Avramenko M, Zhigunov D, Smirnova N. Large-scale synthesis of ZnO nanostructures by pulse electrochemical method and their photocatalytic properties[J]. Mater. Sci. Semicond. Process, 2018, 76: 7–13.

[27] Ulyankina A, Molodtsova T, Gorshenkov M, Leontyev I, Zhigunov D, Konstantinova E, Lastovina T, Tolasz J, Henych J, Licciardello N, Cuniberti G, Smirnova N. Photocatalytic degradation of ciprofloxacin in water at nano-ZnO prepared by pulse alternating current electrochemical synthesis[J]. J. Water Process. Eng., 2021, 40: 101809.

[28] Ulyankina A, Tsarenko A, Yatsenko A, Gorshenkov M, Smirnova N. Photo(electro)catalytic performance of ZnO-based nanopowders prepared through pulse alternating current electrosynthesis in alkaline earth chloride electrolytes[J]. ChemistrySelect, 2023, 8(37): e202300457.

[29] Tsarenko A, Gorshenkov M, Yatsenko A, Zhigunov D, Butova V, Kaichev V, Ulyankina A. Electrochemical synthesis-dependent photoelectrochemical properties of tungsten oxide powders[J]. Chemengineering, 2022, 6(2): 31.

[30] Ulyankina A, Tsarenko A, Molodtsova T, Yatsenko A, Gorshenkov M, Kaichev V, Kuriganova A, Smirnova N. Tungsten oxide nanopowders: pulse alternating current electrosynthesis, structure optimization and performance in a flow photocatalytic fuel cell[J]. J. Mater. Sci., 2023, 58(27): 11187–11197.

[31] Ulyankina A, Avramenko M, Kusnetsov D, Firestein K, Zhigunov D, Smirnova N. Electrochemical synthesis of TiO_2 under pulse alternating current: effect of thermal treatment on the photocatalytic activity[J]. ChemistrySelect, 2019, 4(6): 2001–2007.

[32] Molodtsova T A, Kuriganova A B, Fesenko L N, Leontyev I N, Smirnova N V. Optimization of *c/rh* -In $_2O_3$-based electrode technology for photoelectrochemical systems[J]. Kinet. Catal., 2024, 65(5): 597–604.

[33] Ulyankina A A, Kuriganova A B, Smirnova N V. Photocatalytic properties of SnO_2-SnO nanocomposite prepared via pulse alternating current synthesis[J]. Mendeleev Commun., 2019, 29(2): 215–217.

[34] Molodtsova T, Gorshenkov M, Kolesnikov E, Leontyev I, Kaichev V, Zhigunov D, Faddeev N, Kuriganova A, Smirnova N. Fabrication of nano-In_2O_3 phase junction by pulse alternating current synthesis for enhanced photoelectrochemical performance: unravelling the role of synthetic conditions[J]. Ceramics Int., 2023, 49(7): 10986–10992.

[35] Kuriganova A B, Smirnova N V, Leontyev I N, Avramenko M V. Investigation of structural, microstructural and electrochemical characteristics of Pt/SnO_x-C electrocatalysts prepared via electrochemical dispersion of tin and platinum[J]. ChemChemTech, 2019, 62(9): 53–59.

[36] Kuriganova A B, Leontyev I N, Avramenko M V, Faddeev N A, Smirnova N V. Graphene structures prepared via pulse alternating current technique[J]. Mendeleev Commun., 2022, 32(3): 308–310.

[37] Kuriganova A B, Leontyev I N, Avramenko M V, Popov Y, Maslova O A, Koval O Y, Smirnova N V. One-step simultaneous synthesis of graphene and Pt nanoparticles under the action of pulsed alternating current and electrochemical performance of Pt/graphene catalysts[J]. ChemistrySelect, 2017, 2(24): 6979–6983.

[38] Kuriganova A, Kubanova M, Leontyev I, Molodtsova T, Smirnova N. Pulse electrolysis technique for preparation of bimetal tin-containing electrocatalytic materials[J]. Catalysts, 2022, 12(11): 1444.

[39] Kuriganova A, Leontyeva D, Ivanov S, Bund A, Smirnova N. Electrochemical dispersion technique for preparation of hybrid MOx-C supports and Pt/MOx-C electrocatalysts for low-temperature fuel cells[J]. J. Appl. Electrochem., 2016, 46(12): 1245–1260.

[40] Kuriganova A B, Smirnova N V. Pt/SnO_x-C composite material for electrocatalysis[J]. Mendeleev Commun., 2014, 6(24): 351–352.

[41] Rudi S, Cui C, Gan L, Strasser P. Comparative study of the electrocatalytically active surface areas (ECSAs) of Pt alloy nanoparticles evaluated by hupd and CO-stripping voltammetry[J]. Electrocatal., 2014, 5(4): 408–418.

[42] Metikoš-Huković M, Omanović S. Kinetics of anodic oxide-film growth on tin: ionic transport across a barrier in the high-field limit[J]. Mater. Chem. Phys., 1994, 38(1): 55–62.

[43] Palacios-Padrós A, Caballero-Briones F, Díez-Pérez I, Sanz F. Tin passivation in alkaline media: formation of SnO microcrystals as hydroxyl etching product[J]. Electrochim. Acta, 2013, 111: 837–845.

[44] Kuriganova A B, Brink I Y, Smirnova N. Theoretical and technological fundamentals of pulse electrolysis for the production of electro- and catalytically active materials based on Pt, Pd, Sn and graphene nanostructures[J]. Nano Mater. Sci., 2024. https://doi.org/10.1016/j.nanoms.2024.09.007.

[45] Abrahams I, Grimes S M, Johnston S R, Knowles J C. Ti (II) oxyhydroxide by X-ray powder diffraction[J]. Acta Crystallogr., Sect. C: Cryst. Struct. Commun., 1996, 52(2): 286–288.

[46] Tian F, Wang X B, Chen Z Y, Guo Y M, Liang H J, Lu Z S, Wang D, Lou X, Yang L. A facile post-process method to enhance crystallinity and electrochemical properties of SnO_2/rGO composites with three-dimensional hierarchically porous structure[J]. RSC Adv., 2016, 6(108): 106275–106284.

[47] Kim W J, Lee S W, Sohn Y. Metallic Sn spheres and SnO_2@C core-shells by anaerobic and aerobic catalytic ethanol and CO oxidation reactions over SnO_2 nanoparticles[J]. Sci. Rep., 2015, 5: 513448.

[48] Thommes M, Kaneko K, Neimark Alexander V, Olivier James P, Rodriguez-Reinoso F, Rouquerol J, Sing Kenneth S W. Physisorption of gases, with special reference to the evaluation of surface area and pore size distribution (IUPAC Technical Report)[J]. Pure Appl. Chem., 2015, 87(9–10): 1051–1069.

[49] Xin F, Whittingham M S. Challenges and development of tin-based anode with high volumetric capacity for Li-ion batteries[J]. Electrochem. Energy Rev., 2020, 3(4): 643–655.

[50] Kuriganova A B, Vlaic C A, Ivanov S, Leontyeva D V, Bund A, Smirnova N V. Electrochemical dispersion method for the synthesis of SnO_2 as anode material for lithium ion batteries[J]. J. Appl. Electrochem., 2016, 46(5): 527–538.

[51] Shin J H, Song J Y. Electrochemical properties of Sn-decorated SnO nanobranches as an anode of Li-ion battery[J]. Nano Converg., 2016, 3(1): 9.

[52] Long Z Q, Li Q G, Wei T, Zhang G M, Ren Z J. Historical development and prospects of photocatalysts for pollutant removal in water[J]. J. Hazard. Mater., 2020, 395: 122599.

[53] Byrne C, Subramanian G, Pillai S C. Recent advances in photocatalysis for environmental applications[J]. J. Environ. Chem. Eng., 2018, 6(3): 3531–3555.

[54] Santhi K, Rani C, Karuppuchamy S. Synthesis and characterization of a novel SnO/SnO_2 hybrid photocatalyst[J]. J. Alloys Compd., 2016, 662: 102–107.

[55] Roy A, Arbuj S, Waghadkar Y, Shinde M, Umarji G, Rane S, Patil K, Gosavi S, Chauhan R. Concurrent synthesis of SnO/SnO_2 nanocomposites and their enhanced photocatalytic activity[J]. J. Solid State Electrochem., 2017, 21(1): 9–17.

[56] Bhattacharjee A, Ahmaruzzaman M, Devi T B, Nath J. Photodegradation of methyl violet 6B and methylene blue using tin-oxide nanoparticles (synthesized via a green route)[J]. J. Photochem. Photobiol. A, 2016, 325: 116–124.

[57] Abdelkader E, Nadjia L, Naceur B, Noureddine B. SnO_2 foam grain-shaped nanoparticles: synthesis, characterization and UVA light induced photocatalysis[J]. J. Alloys Compd., 2016, 679: 408–419.

[58] Lin J J, Luo Z Z, Liu J J, Li P. Photocatalytic degradation of methylene blue in aqueous solution by using ZnO-SnO_2 nanocomposites[J]. Mater. Sci. Semicond. Process, 2018, 87: 24–31.

[59] Wasmus S, Küver A. Methanol oxidation and direct methanol fuel cells: a selective review[J]. J. Electroanal. Chem., 1999, 461(1–2): 14–31.

[60] Munjewar S S, Thombre S B, Mallick R K. Approaches to overcome the barrier issues of passive direct methanol fuel cell–Review[J]. Renew. Sust. Energ. Rev., 2017, 67: 1087–1104.

[61] Alias M, Kamarudin S, Zainoodin A, Masdar M. Active direct methanol fuel cell: an overview[J]. Int. J. Hydrogen Energy, 2020, 45(38): 19620–19641.

[62] Kamarudin M, Kamarudin S, Masdar M, Daud W. Direct ethanol fuel cells[J]. Int. J. Hydrogen Energy, 2013, 38(22): 9438–9453.

[63] Badwal S, Giddey S, Kulkarni A, Goel J, Basu S. Direct ethanol fuel cells for transport and stationary applications–A comprehensive review[J]. Appl. Energy, 2015, 145: 80–103.

[64] Mussatto S I, Dragone G, Guimarães P M R, Silva J P A, Carneiro L M, Roberto I C, Vicente A, Domingues L, Teixeira J A. Technological trends, global market, and challenges of bio-ethanol production[J]. Biotechnol. Adv., 2010, 28(6): 817–830.

[65] Willsau J, Heitbaum J. Elementary steps of ethanol oxidation on Pt in sulfuric acid as evidenced by isotope labelling[J]. J. Electroanal. Chem. Interfacial Electrochem., 1985, 194(1): 27–35.

[66] Iwasita T, Pastor E. A DEMS and FTIR spectroscopic investigation of adsorbed ethanol on polycrystalline platinum[J]. Electrochim. Acta, 1994, 39(4): 531–537.

[67] Bittins-Cattaneo B, Wilhelm S, Cattaneo E, Buschmann H, Vielstich W. Intermediates and products of ethanol oxidation on platinum in acid solution[J]. Ber. Bunsenges. Phys. Chem., 1988, 92(11): 1210–1218.

[68] Hitmi H, Belgsir E, Léger J M, Lamy C, Lezna R. A kinetic analysis of the electro-oxidation of ethanol at a platinum electrode in acid medium[J]. Electrochim. Acta, 1994, 39(3): 407–415.

[69] Gootzen J, Visscher W, Van Veen J. Characterization of ethanol and 1, 2-ethanediol adsorbates on platinized platinum with Fourier transform infrared spectroscopy and differential electrochemical mass spectrometry[J]. Langmuir, 1996, 12(21): 5076–5082.

[70] Schmidt V M, Ianniello R, Pastor E, González S. Electrochemical reactivity of ethanol on porous Pt and PtRu: oxidation/reduction reactions in 1 M $HClO_4$[J]. J. Phys. Chem., 1996, 100(45): 17901–17908.

[71] Marinkovic N S, Li M, Adzic R R. Pt-based catalysts for electrochemical oxidation of ethanol[J]. Top Curr. Chem. (Z), 2019, 377(11): 1–39.

[72] Huang H, Blackman O F, Celorrio V, Russell A E. Isolating the contributions of surface Sn atoms in the bifunctional behaviour of PtSn CO oxidation electrocatalysts[J]. Electrochim. Acta, 2021, 390: 138811.

[73] Kuriganova A, Leontyev I, Leontyev N, Smirnova N. Pt Catalysts prepared via top-down electrochemical approach: synthesis methodology and support effects[J]. J. Electrochem. Sci. Technol., 2024, 15(3): 345–352.

[74] Díaz R, Díez-Pérez I, Gorostiza P, Sanz F, Morante J R. An electrochemical study of tin oxide thin film in borate buffer solutions[J]. J. Braz. Chem. Soc., 2003, 14(4): 523–529.

[75] Abd El Wahae F, Abd El Kader J, El Shayeb H, El Din A S. On the pitting corrosion of tin in aqueous solutions[J]. J. Corrosion Science, 1978, 18(11): 997–1009.

[76] Morgan Tench D, Anderson D, Kim P. Solderability assessment via sequential electrochemical reduction analysis[J]. J. Appl. Electrochem., 1994, 24(1): 18–29.

[77] Cho S, Yu J, Kang S K, Shih D Y. Oxidation study of pure tin and its alloys via electrochemical reduction analysis[J]. J. Electron. Mater., 2005, 34(5): 635–642.

[78] Alvarez P, Ribotta S, Folquer M, Gervasi C, Vilche J. Potentiodynamic behaviour of tin in different buffer solutions[J]. Corrosion Sci., 2002, 44(1):49–65.

[79] Begum S N, Basha A, Muralidharan V, Lee C W. Electrochemical behaviour of tin in alkali solutions containing halides[J]. Mater. Chem. Phys., 2012, 132(2–3): 1048–1052.

[80] Trompette J L. The comparative breakdown of passivity of tin by fluorides and chlorides interpreted through the 'law of matching affinities' concept[J]. Corrosion Sci., 2015, 942: 88–93.

[81] Collins K D, Neilson G W, Enderby J E. Ions in water: characterizing the forces that control chemical processes and biological structure[J]. Biophys. Chem., 2007, 128(2): 95–104.

[82] Collins K D. Ions from the Hofmeister series and osmolytes: effects on proteins in solution and in the crystallization process[J]. Methods, 2004, 34(3): 300–311.

[83] Perrin D D, Dempsey B, Serjeant E P. pKa prediction for organic acids and bases[M]. Springer, 1981, Vol. 1.

[84] Ghosh S, Roy S. Effect of ageing on $Sn_6O_4(OH)_4$ in aqueous medium—simultaneous production of SnO and SnO_2 nanoparticles at room temperature[J]. J. Solgel Sci. Technol., 2017, 81(3): 769–773.

[85] Marcus Y. Thermodynamics of solvation of ions. Part 5. Gibbs free energy of hydration at 298.15 K[J]. J. Chem. Soc., Faraday trans., 1991, 87(18): 2995–2999.

[86] Pauling L. The nature of the chemica bond. IV. The energy of single bonds and the relative electronegativity of atoms[J]. J. Am. Chem. Soc., 1932, 54(9): 3570–3582.

[87] Nakashima T., Fujishima A. Adsorption of anionic and cationic dyes in dilute solutions onto a SnO_2 surface measured by total internal reflection fluorescence[J]. Ber. Bunsenges. Phys. Chem., 1995, 99: 609–616.

[88] Séby F, Potin-Gautier M, Giffaut E, Donard O F X. A critical review of thermodynamic data for inorganic tin species[J]. Geochim. Cosmochim. Acta, 2001, 65(18): 3041–3053.

调控锡氧化物基材料功能特性的新见解

Alexandra Kuriganova*, Nina Smirnova
普拉托夫南俄罗斯国立理工大学, 新切尔卡斯克, 俄罗斯

摘要:

开发纳米结构材料微观特性和组成可控的制备方法, 是发展具有明确功能特性材料制备技术的重要基础。脉冲电解法, 一种自上而下的电化学方法, 已被证明是制备纳米结构材料的可行方法, 对合成锡氧化物基材料尤其有效。这种方法通过改变水性电解质的阴离子成分, 可以有效地控制锡氧化物颗粒产物的组成和形状, 从而避免在合成过程中使用额外的封端剂, 并省去高温后处理步骤。本文结果表明, 脉冲电解法得到的锡氧化物的组成和微观结构特性取决于氟化锡和氯化锡络合物不同的稳定性, 以及氯化阴离子和氟化阴离子与锡氧化物表面不同的相互作用机制, 并受到这些卤素阴离子不同的各向同性/各向混杂性的影响。该方法所获得的分散性锡氧化物的组成和微观结构特征决定了它们作为锂离子电池负极材料、光催化剂或铂基电催化剂混合载体亲氧组分的潜在应用。

关键词: 锡氧化物;脉冲电解;锂离子电池;光催化;燃料电池